

# Preparation and coherent manipulation of pure quantum states of a single molecular ion

Chin-wen Chou<sup>1</sup>, Christoph Kurz<sup>1,2</sup>, David B. Hume<sup>1</sup>,  
Philipp N. Plessow<sup>3</sup>, David R. Leibbrandt<sup>1,2</sup>, and Dietrich Leibfried<sup>1</sup>

<sup>1</sup>*Time and Frequency Division, National Institute of  
Standards and Technology, Boulder, Colorado 80305, USA*

<sup>2</sup>*University of Colorado, Boulder, Colorado, USA and*

<sup>3</sup>*Institute of Catalysis Research and Technology,  
Karlsruhe Institute of Technology, Karlsruhe, Germany*

(Dated: December 9, 2024)

## Abstract

After remarkable progress with laser cooled atoms in diverse fields from atomic clocks to quantum information processing, physicists are exploring a next frontier: ultracold molecules. While these systems could lead to profound developments, for example probing the predictions of fundamental theories and realizing controlled chemical reactions, the vibrational and rotational degrees of freedom in molecules pose a formidable challenge for preparation and manipulation of their quantum mechanical states. The complicated molecular level structures render the highly successful methods in atomic physics inapplicable to most molecules. Here, we demonstrate a general protocol for preparation, manipulation, and nondestructive detection of quantum mechanical states in single molecular ions. Our work provides a versatile toolbox for the study of a broad range of molecular ions, adding to the capabilities developed in atomic physics over the last several decades. This opens the path to applications in fundamental physics, metrology, and quantum control.

Laser cooling and trapping of atoms and atomic ions has led to breakthroughs in understanding of exotic phases of matter [1–5], development of exquisite sensors [6] and state-of-the-art atomic clocks [7]. Continuing such progress, precision experiments with cold trapped molecules offer unique opportunities in numerous fields [8] from physical chemistry to precision metrology [9–12] and quantum information science [13, 14]. However, due to their more complicated internal structure, achieving the same level of measurement precision and quantum-state control with molecules has been realized only in a very limited number of settings [15, 16] and never for individual molecular ions. Previous experiments relied on fortuitous molecular properties [17], dedicated multi-laser systems [18] or sophisticated laser cooling techniques [15]. In the case of a molecular ion, its charge provides a means of trapping and sympathetically cooling via its Coulomb interaction with a co-trapped atomic ion that is readily laser-cooled [19]. With these features, various crucial steps towards coherent spectroscopy of trapped molecular ions, such as non-destructive state detection [20] and cooling to the rotational ground state [17], have been demonstrated. However, coherent control of the quantum state of a molecular ion has not yet been achieved. Furthermore, the laser systems previously used for state preparation were tailored to the specific level structures of the molecules under study and thus required different lasers when changing the molecular ion species under study.

Here, we demonstrate a general protocol for coherent manipulation of trapped molecular ions in their electronic and vibrational ground states based on quantum-logic spectroscopy [21] and stimulated Raman transitions (SRTs) driven by a far-detuned laser source [22, 23]. Because the rotational motion is not cooled, our approach relies on probabilistically preparing a particular rotational state via a projective measurement. We cool the shared motion of the molecular ion and a co-trapped atomic ion in the harmonic trapping potential to the ground state [24]. Then we set the relative detuning of the Raman beams to drive a specific transition in the molecule in such a way that a state change of the molecule is accompanied by an excitation of the shared motion (motional sideband). We can efficiently detect this excitation with the atomic ion, which projects the molecule into the final state of the attempted transition, leaving the molecule in a known, pure quantum state. This allows for subsequent coherent manipulation of the molecular state, as well as spectroscopy of molecular transitions. In addition, we pump the molecular ion into specific sublevels of its rotational states by directional transfer of angular momentum from the photons that

are absorbed and emitted during a Raman transition, effectively orienting the molecular rotation along an axis of our choice. The improved orientation after pumping increases the state preparation success rate and the signal-to-noise ratio in subsequent experiments.

In our experiments, we trap two  $^{40}\text{Ca}^+$  ions in a harmonic ion trap in ultra-high vacuum at room temperature ( $P \sim 4 \times 10^{-9}$  Pa). To form the molecular ion, hydrogen gas is leaked into the vacuum chamber until one of the  $^{40}\text{Ca}^+$  ions reacts to form a  $^{40}\text{CaH}^+$  ion [25]. The  $^{40}\text{CaH}^+$  molecular ion serves as a convenient test case for a much wider class of molecules that could be generated by various other techniques, co-trapped with atomic ions and manipulated by the techniques described below. The  $^{40}\text{Ca}^+$  ion, which can be readily laser cooled, optically pumped, and manipulated [26], is coupled to the molecule by mutual Coulomb repulsion so that the shared normal modes of translational motion between the ions can be sympathetically cooled to their ground state [19, 20, 24]. To realize efficiently shared normal modes, which are crucial for our experiments, the two singly-charged positive ions should roughly be within a mass ratio of three [22]. The  $^{40}\text{CaH}^+$  quickly relaxes to its singlet electronic and vibrational ground state, but remains in a mixture of rotational states, in equilibrium with the blackbody radiation of its room temperature environment. A simplified diagram of the experimental setup is shown in Fig. 1.

The energies of the rotational levels of the molecule referenced to the electronic and vibrational ground state are approximately proportional to the eigenvalues of the square of the rotational angular momentum operator,  $\mathbf{J}^2$ , namely  $\hbar R \cdot J(J+1)$ , with rotational constant  $R \simeq 2\pi \times 144$  GHz for  $^{40}\text{CaH}^+$  [29] and rotational quantum numbers  $J \in \{0, 1, 2, \dots\}$ . For a given  $J$  and with a magnetic field  $\mathbf{B}$  of approximate magnitude 0.36 mT applied as indicated in Fig. 1, the energy of a state is further determined by the mutual (hyperfine) coupling between the orbital magnetic moment, produced by the charges rotating with the molecule, and the magnetic moment of the hydrogen nucleus ( $\propto \mathbf{J} \cdot \mathbf{I}$ ), as well as the coupling of the individual magnetic moments to the external magnetic field ( $\propto \mathbf{J} \cdot \mathbf{B}$  and  $\propto \mathbf{I} \cdot \mathbf{B}$ ) which split the levels by a few kilohertz. Here  $\mathbf{I}$  is the operator of the proton spin. We can classify the eigenstates by  $|\mathcal{J}\rangle \equiv |J, m, \xi\rangle$ , where  $\mathcal{J}$  stands for the set of quantum numbers  $\{J, m, \xi\}$  and  $m \in \{-J - 1/2, -J + 1/2, \dots, J + 1/2\}$  denotes the sum  $m = m_J + m_I$  of the components of the rotational angular momentum and the proton spin along  $\mathbf{B}$ . The value of  $m$  is a good quantum number for arbitrary  $\mathbf{B}$ . The last label  $\xi \in \{+, -\}$  indicates one of the two eigenstates that can be formed by the superposition of

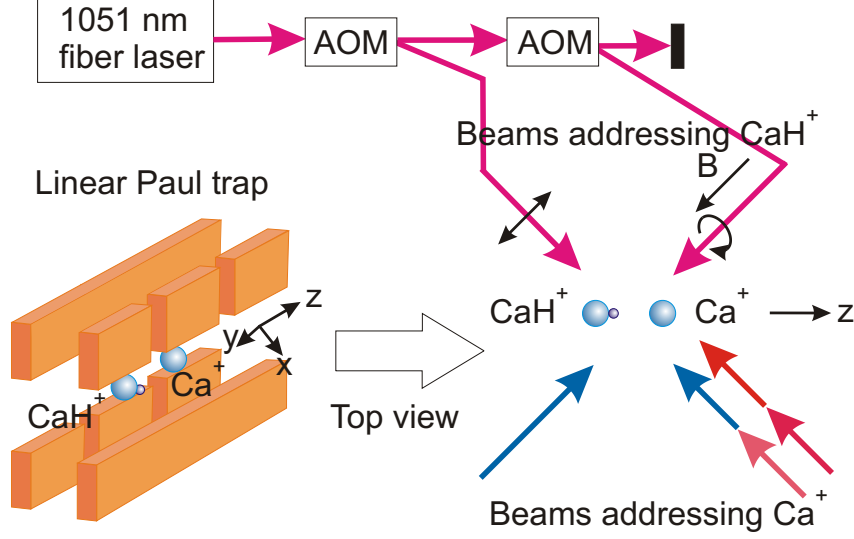


FIG. 1. Simplified experimental setup: A  $^{40}\text{CaH}^+$ - $^{40}\text{Ca}^+$  ion pair is held in a linear Paul trap. Two modes of motion in the  $z$  direction and one in the  $x$  direction of the ion pair are prepared in the motional ground states via laser cooling on  $^{40}\text{Ca}^+$ . The motional mode in the  $z$  direction in which the two ions oscillate out of phase is used as the normal mode for the quantum-logic spectroscopy protocol. Two Raman beams derived from a single fiber laser are split in frequency by two acousto-optic modulators (AOMs). They are directed onto the molecular ion with a  $k$ -vector difference along the trap  $z$  axis. The two Raman beams have  $\pi$  and  $\sigma^-$  polarizations relative to the quantization axis defined by the applied magnetic field. They drive either carrier two-photon stimulated-Raman transitions in the molecule, or their motional sidebands, depending on the frequency detuning, while changing the projection quantum number  $m$  of the molecular angular momentum by  $\pm 1$ . Single quanta of excitation in the ion motion can be detected by driving sidebands of the narrow quadrupole transition between the  $4s^2S_{1/2}$  and  $3d^2D_{5/2}$  levels of the  $^{40}\text{Ca}^+$  atomic ion, followed by electron shelving detection with the laser beams addressing  $^{40}\text{Ca}^+$  (see text and Supplementary Information). Detection of motional excitation on the  $^{40}\text{Ca}^+$  ion projects the molecule into the final state of the addressed transition, which is then available for further manipulation.

product states with the same  $m$  but opposite proton spin,  $|J, m_J = m + 1/2\rangle|m_I = -1/2\rangle$  and  $|J, m_J = m - 1/2\rangle|m_I = +1/2\rangle$ , with amplitudes of superposition depending on the value of  $\mathbf{B}$  (see Supplementary Information). In the extreme states where spin and rotational angular momentum are aligned with the quantization axis, the eigenstates are simple product states

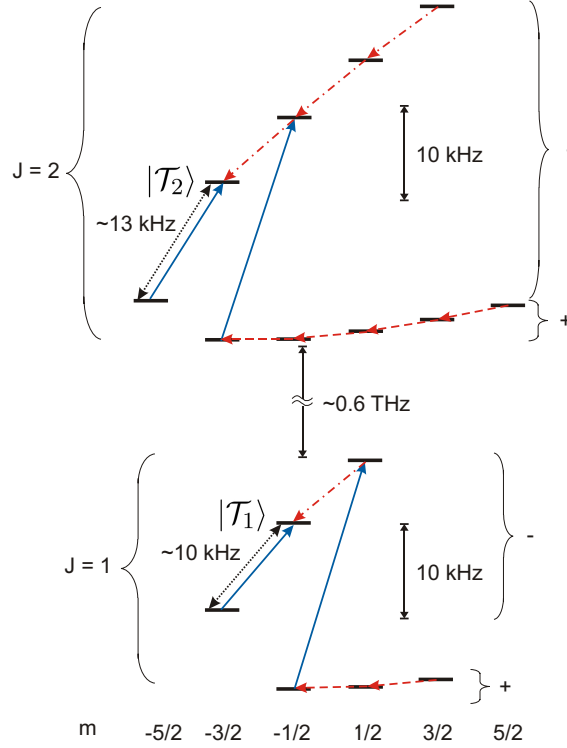


FIG. 2. The level diagrams for the rotational levels of  $^{40}\text{CaH}^+$  for  $J \in \{1, 2\}$  according to our model of the hyperfine structure of  $^{40}\text{CaH}^+$  (see Supplementary Information). At  $|\mathbf{B}| \simeq 0.36$  mT, the energy eigenstates  $|J, m, \pm\rangle$  are either superpositions of product states of rotation and nuclear spin sublevels adding to the same total  $m$ , or extreme states where the proton spin and the rotation are aligned ( $m = \pm(J + 1/2)$ ). The red dashed, red dot-dashed, and blue solid arrows indicate the directionality of the pumping transitions for population concentration. Red dashed and dot-dashed arrows indicate that several transitions can be addressed simultaneously within the spectral resolution of the pumping sequence, while blue arrows indicate transitions that uniquely identify the involved states. The black dotted arrows show the  $|\mathcal{T}_J\rangle = |J, -J + 1/2, -\rangle \leftrightarrow |J, -J - 1/2, -\rangle$  target transitions with unique frequencies that are driven for the projective pure state preparation and coherent manipulation (see text).

$|J, \pm(J+1/2), \pm\rangle = |J, m_J = \pm J\rangle|m_I = \pm 1/2\rangle$  and the label  $\xi$  denotes the sign of  $\pm(J+1/2)$ . We operate at an intermediate magnetic field where all three coupling terms lead to energy shifts of similar magnitude. The calculated energy levels corresponding to the eigenstates are displayed in Fig. 2 for  $J \in \{1, 2\}$ .

To drive the SRTs in the molecule, we derive two Raman beams from a fiber laser at approximately 1051 nm with two acousto-optic modulators (AOMs) driven at different frequencies. That enables us to pulse each beam with variable amplitude and to set their frequency difference precisely. The two beams are directed separately onto the ions, one circularly polarized ( $\sigma^-$ ), the other linearly ( $\pi$ ) with respect to the quantization axis along the magnetic field, as indicated in Fig. 1. With  $\Delta\nu \equiv \nu_\sigma - \nu_\pi$  tuned near  $\pm(E_f - E_i)/h$  and  $\pm[(E_f - E_i)/h \pm \nu_t]$  (as required by energy conservation), they can coherently drive carrier two-photon SRTs and the first sidebands of translational motion, respectively. Here  $\nu_\sigma$  ( $\nu_\pi$ ) is the frequency of the  $\sigma^-$  ( $\pi$ ) polarized beam,  $E_i$  ( $E_f$ ) is the energy of the initial (final) molecular level, and  $\nu_t$  is the frequency of the motional mode. In our current Raman beam setup,  $|\Delta\nu|$  is limited to be  $< 10$  MHz, so we can only drive SRTs between molecular levels with the same  $J$ . To minimize the perturbation on the molecular energy levels caused by the Raman beams, we control the intensity ratio between the  $\sigma^-$  and  $\pi$  beams to minimize the differential AC Stark shifts between the molecular levels (see Supplementary Information).

In the protocol of quantum-logic spectroscopy, the information regarding whether the molecular ion undergoes a SRT can be imprinted on a normal mode of motion shared between the molecule and an atomic ion and later read out via the atomic ion. In a first-order blue sideband transition, the SRT excites the harmonic motion of the ions in the trap potential, adding a phonon to the mode. Similarly, a red sideband transition subtracts a phonon from the mode. If the harmonic motion is cooled to the ground state, the red sideband, which requires that a quantum is transferred from the motion to the photon energy, cannot be driven. However, a blue sideband of a transition in the molecule can still be driven, leaving a quantum of motion behind in the normal mode. That event can be detected by driving the red sideband of the narrow quadrupole transition between the  $4s^2S_{1/2}$  and  $3d^2D_{5/2}$  levels of the  $^{40}\text{Ca}^+$  atomic ion, which alters the state of the  $^{40}\text{Ca}^+$  conditioned on the existence of the quantum of motion, followed by fluorescence detection. High detection fidelity can be achieved in a single shot by simply checking the resultant photon counts against a pre-determined threshold (see Supplementary Information and [27, 28]).

The probabilistic projective preparation of a pure quantum state in the molecular ion proceeds as follows. If we assume perfect ground state cooling, with the  $^{40}\text{Ca}^+$  prepared in  $|D\rangle$ , the  $D_{5/2}$ ,  $m = -5/2$  state, the density matrix of the molecule, the normal mode, and

the atomic ion can be written as

$$\rho_0 = \left( \sum_{\mathcal{J}} P_{\mathcal{J}} |\mathcal{J}\rangle \langle \mathcal{J}| \right) |0\rangle \langle 0| |D\rangle \langle D|, \quad (1)$$

where  $P_{\mathcal{J}}$  is the population in any state  $|\mathcal{J}\rangle$ , which is less than 1.1 % when in equilibrium with blackbody radiation at 300 K, and  $|n\rangle$  denotes the motional state with  $n$  phonons in the normal mode. With probability  $P_{\mathcal{J}_i}$ , the molecule is in  $|\mathcal{J}_i\rangle$  and we can drive the molecular blue sideband transition  $|\mathcal{J}_i\rangle|0\rangle|D\rangle \rightarrow (\alpha|\mathcal{J}_i\rangle|0\rangle + \beta|\mathcal{J}_f\rangle|1\rangle)|D\rangle$ , where  $\alpha$  and  $\beta$  are amplitudes determined by the pulse duration and the detuning with  $|\alpha|^2 + |\beta|^2 = 1$ . If the  $\sigma^-$  ( $\pi$ ) photon in the SRTs has to be absorbed to satisfy energy conservation, conservation of angular momentum requires that  $m_f = m_i - 1$  ( $m_f = m_i + 1$ ). If the  $|\mathcal{J}_i\rangle \leftrightarrow |\mathcal{J}_f\rangle$  transition has a unique frequency in the molecule, the density matrix of the system is modified to

$$\begin{aligned} \rho_1 = & P_{\mathcal{J}_i} (\alpha|\mathcal{J}_i\rangle|0\rangle + \beta|\mathcal{J}_f\rangle|1\rangle) (\alpha^*\langle\mathcal{J}_i|\langle 0| + \beta^*\langle\mathcal{J}_f|\langle 1|) |D\rangle \langle D| \\ & + \sum_{\mathcal{J} \neq \mathcal{J}_i} P_{\mathcal{J}} |\mathcal{J}\rangle \langle \mathcal{J}| |0\rangle \langle 0| |D\rangle \langle D|. \end{aligned} \quad (2)$$

At this point we can attempt to drive a  $\pi$ -pulse on the red sideband of  $^{40}\text{Ca}^+$ , which induces the transition  $|1\rangle|D\rangle \rightarrow |0\rangle|S\rangle$ , where  $|S\rangle$  denotes the  $S_{1/2}$ ,  $m = -1/2$  state of  $^{40}\text{Ca}^+$ . Fluorescence detection on the  $^{40}\text{Ca}^+$  distinguishes  $|S\rangle$ , which scatters many photons, from  $|D\rangle$ , which ideally scatters no photons. Thus, with probability  $P_{\mathcal{J}_i}|\beta|^2$  the density matrix of the molecule is projected to the pure state

$$\rho_M = |\mathcal{J}_f\rangle \langle \mathcal{J}_f|, \quad (3)$$

which is heralded non-destructively by detecting that the  $^{40}\text{Ca}^+$  ion scatters photons. The probability of this event is proportional to  $|\beta|^2$ . Therefore, we can measure Raman spectra of molecular transitions by recording the probability of detecting  $|S\rangle$ , as long as we leave the molecule enough time to re-establish equilibrium with the blackbody environment, so that  $P_{\mathcal{J}_i}$  is the same for every attempt. Such a spectrum with  $m_f = m_i - 1$  is shown as the blue curve in Fig. 3. Due to the small magnitudes of  $P_{\mathcal{J}}$ , the transitions with frequencies  $\omega/2\pi \equiv (E_f - E_i)/h$  between  $-10$  and  $-50$  kHz are not discernible from measurement noise, which we have optimized to be at the 0.5 % level (see Supplementary Information). Peaks between  $0$  and  $-10$  kHz are visible because they arise from a large number of sublevels. The peak corresponding to  $\omega/2\pi = 0$  is attributed to coherent motion that can be driven by

modulated optical dipole forces without changing the internal state of the molecule if the polarization of the Raman beams is not perfect on both ions.

In order to achieve a better signal-to-noise level in the target transitions with unique frequencies ( $|J, -J + 1/2, -\rangle \leftrightarrow |J, -J - 1/2, -\rangle$  in this work), it is beneficial to increase the populations in the corresponding initial states over the thermal equilibrium levels. Since the blackbody relaxation times ( $\sim 100$  ms to  $> 2$  s at 300 K for  $J < 8$ ) are long compared with attempts to drive transitions ( $< 5$  ms), we can concentrate the population in an initial pumping stage. The pumping uses a pulse sequence similar to projective state preparation. The ions are first cooled to the ground state of motion, then a blue sideband pulse is applied to the molecular transition to be pumped. Further ground state cooling produces dissipation in the system, making these pumping transitions directional [21], in analogy to a typical optical pumping process where spontaneous decay removes entropy from the system. The effect of pumping in the molecular system can be understood by returning to Eq. (2), which describes the density matrix of the system after the blue sideband pumping pulse on the molecular ion. In this case  $J_i$  denotes the state being pumped. If  $|\beta| \neq 0$  after the pumping attempt, the sideband cooling pulses on the  $^{40}\text{Ca}^+$  destroy the coherence induced from driving the molecular blue sideband transition, transforming the density matrix from  $\rho_1$  to

$$\rho_2 = \left[ P_{\mathcal{J}_i} |\alpha|^2 |\mathcal{J}_i\rangle\langle\mathcal{J}_i| + (P_{\mathcal{J}_i} |\beta|^2 + P_{\mathcal{J}_f}) |\mathcal{J}_f\rangle\langle\mathcal{J}_f| + \sum_{\mathcal{J} \neq \mathcal{J}_i, \mathcal{J}_f} P_{\mathcal{J}} |\mathcal{J}\rangle\langle\mathcal{J}| \right] |0\rangle\langle 0| |D\rangle\langle D|. \quad (4)$$

The population of  $|\mathcal{J}_i\rangle$  is decreased to  $P_{\mathcal{J}_i} |\alpha|^2$  while the population of  $|\mathcal{J}_f\rangle$  is increased to  $P_{\mathcal{J}_f} + P_{\mathcal{J}_i} |\beta|^2$ . When repeating this sequence on the transitions indicated by the blue solid, red dashed, and red dot-dashed arrows in Fig. 2, the directionality of angular momentum transfer pumps the population toward the subset of target states which for each  $J \in \{1, 2, 3, \dots\}$  are denoted by the set of quantum numbers  $\mathcal{T}_J = \{J, m = -J + \frac{1}{2}, -\}$ . The population in the  $J = 0$  manifold is not affected because the proton spin cannot be flipped by a SRT. We could pump to a different subset of states by modifying the choice of transitions and their directionality. Note that the quantization axis and beam polarizations can be chosen to orient the rotational axis as well as the proton spin of the resultant pumped molecular state as desired.

For  $^{40}\text{CaH}^+$  in  $|\mathbf{B}| = 0.36$  mT, the frequencies of the transitions  $|J, m, +\rangle \rightarrow |J, m - 1, +\rangle$  and  $|J, m, -\rangle \rightarrow |J, m - 1, -\rangle$ , indicated by the red dashed and dot-dashed arrows in Fig 2,



are in two narrow regions around  $-2$  kHz and  $-6$  kHz, respectively (see Fig. 2 and Fig. 3), thus multiple transitions involving significant population can be simultaneously pumped with one cycle. In order to pump the majority of the population to the target states, transitions with  $\omega/2\pi > 10$  kHz (blue solid arrows in Fig 2) also need to be addressed with additional pumping pulses. Assuming perfect pumping efficiency, the steady state density matrix can be approximated by

$$\rho_p = \left( \frac{1}{2} Q_0 \sum_{J=0} |\mathcal{J}\rangle\langle\mathcal{J}| + \sum_{J>0} Q_J |J, -J + \frac{1}{2}, -\rangle\langle J, -J + \frac{1}{2}, -| \right) |0\rangle\langle 0| |D\rangle\langle D|, \quad (5)$$

where  $Q_J = \sum_{m,\xi} P_{J,m,\xi}$  is the total probability of being in the manifold with rotational quantum number  $J$ , which is increased by a factor  $2(2J+1)$  (the number of sublevels in the manifold) over the probability of being in a certain sublevel  $|J, m, \xi\rangle$  in the equilibrium distribution. The Raman spectrum taken after the pumping stage is shown as the linked red dots in Fig. 3. The target transitions in the molecule (dotted black arrows in Fig. 2) with unique frequencies can thus be mapped out. The transition probabilities for these isolated transitions are significantly increased over the equilibrium spectrum. The  $< 50$  % pumping efficiency could be further improved by optimizing the pumping sequence and duty cycle.

With the increased signals from pumping, the frequencies of the target transitions are identified. The projective state preparation is then achieved by successively driving the  $|\mathcal{T}_J\rangle|0\rangle \rightarrow |J, -J - \frac{1}{2}, -\rangle|1\rangle$  and  $|J, -J - \frac{1}{2}, -\rangle|1\rangle \rightarrow |\mathcal{T}_J\rangle|0\rangle$  sideband transitions with  $\pi$  pulses, interspersed by monitoring the creation and removal of phonons of motion and ground state cooling. Detecting a change in the phonon number heralds the projection of the molecular state into the final level of the sideband transition (see Supplementary Information). This procedure can also be exploited to check whether the molecule is in a certain two-level manifold with pre-determined transition frequencies for the manifolds being monitored. False-positive detection of changes in phonon number can be due to imperfect ground state cooling or heating of the motion from other sources, which impacts the fidelity of the projective state preparation.

After projective state preparation is heralded, the resultant quantum state can be coherently manipulated. We observe Rabi flopping of the molecule by driving the carrier transition  $|\mathcal{T}_J\rangle \leftrightarrow |J, -J - \frac{1}{2}, -\rangle$  for different durations and detecting changes in the molecular state by checking whether  $\pi$  pulses on the sideband transition  $|\mathcal{T}_J\rangle|0\rangle \leftrightarrow |J, -J - \frac{1}{2}, -\rangle|1\rangle$  alter the motional state. To avoid driving multiple transitions, the carrier Raman pulses are reduced

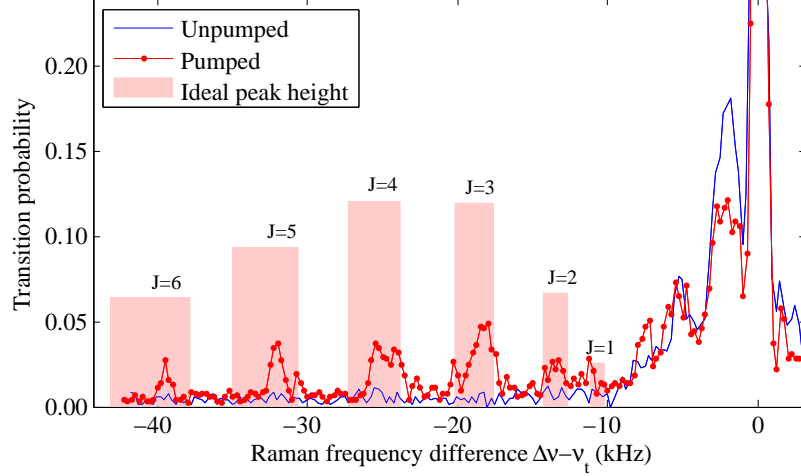


FIG. 3. Raman spectra for  $\Delta m = -1$  blue sideband transitions probed with 1 ms pulses. The frequency axis shows the offset from the motional frequency of the normal mode at  $\sim 5.164$  MHz. The peak at 0 kHz is mainly due to the motion that is directly driven without transitions in the molecule by the optical dipole forces from residual interference between the imperfect polarizations in the two beams. Blue line: without pumping, the two prominent peaks near  $-2$  kHz and  $-6$  kHz correspond to the transitions  $|J, m, \xi\rangle \rightarrow |J, m - 1, \xi\rangle$  which overlap for different  $m$ , for the two cases  $\xi \in \{+, -\}$ , shown by the red dashed and dot-dashed arrows, respectively, in Fig. 2. Red dots: after optical pumping. The peaks near  $\{-11, -14, -19, -25, -32, -40\}$  kHz are identified as the  $|J, -J + \frac{1}{2}, -\rangle \rightarrow |J, -J - \frac{1}{2}, -\rangle$  transitions for  $J \in \{1, 2, 3, 4, 5, 6\}$ , respectively, from their proximity with the predicted frequencies (see Supplementary Information). Pink-shaded bars: the frequencies and heights of the peaks predicted by the theory, with the effect from  $J$ -dependent Rabi rates taken into account. The widths of the bars indicate the ranges of the predicted transition frequencies (see Supplementary Information).

in power by a factor of 10 compared to the sideband pulses. During the coherent evolution, the state of the molecule is ideally

$$|\Psi(t)\rangle = \cos(\Omega_J t) |J, -J - \frac{1}{2}, -\rangle + \sin(\Omega_J t) |\mathcal{T}_J\rangle, \quad (6)$$

where  $\Omega_J$  is the  $J$ -dependent Rabi frequency of the transition. The molecule is detected in  $|\mathcal{T}_J\rangle$  with probability  $C_J \sin^2(\Omega_J t)$  where  $C_J$  is smaller than unity because of inefficiencies in preparation and detection and imperfections in the driving pulse. By repeating preparation, coherent evolution, and state detection we build up sufficient statistics to observe the Rabi

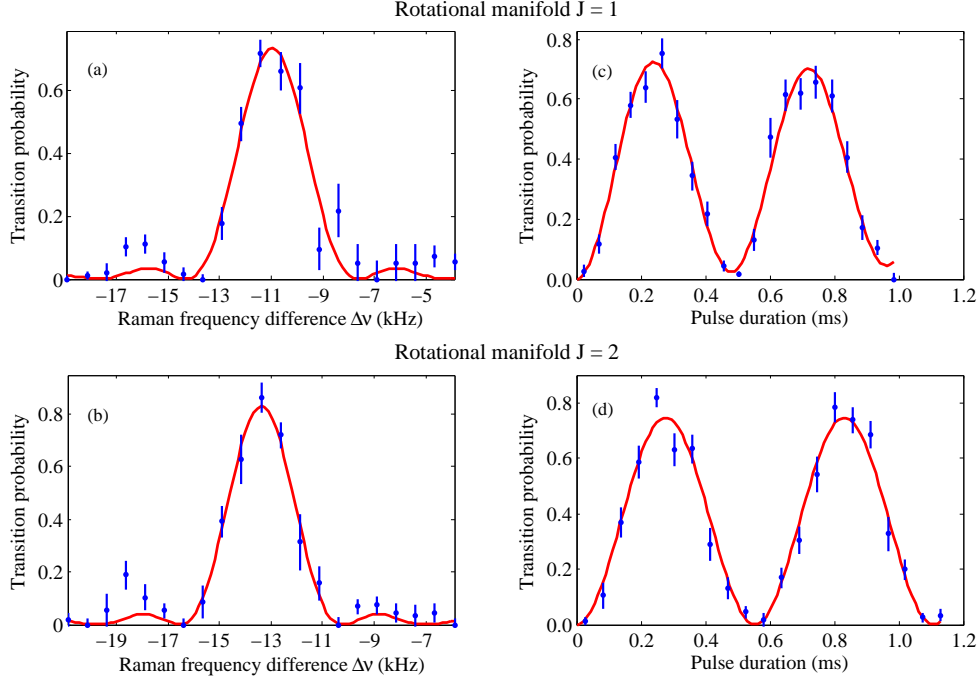


FIG. 4. (a) and (b): Spectra of the transitions  $|J, -J - \frac{1}{2}, -\rangle \leftrightarrow |\mathcal{T}_J\rangle = |J, -J + \frac{1}{2}, -\rangle$ ; (c) and (d): Coherent evolution of the molecular states, where  $J \in \{1, 2\}$ , with adaptive molecular state preparation in  $|J, -J - \frac{1}{2}, -\rangle$ . The red lines in (a) and (b) ((c) and (d)) are the fits to sinc-square functions (sine-squares with exponentially decaying amplitudes).

flops shown in Fig. 4 as a function of Raman pulse durations for  $J \in \{1, 2\}$  (for more details see Supplementary Information).

To further characterize the coherence, we implement a Ramsey sequence, where we first prepare an equally weighted superposition  $(|\mathcal{T}_J\rangle + |J, -J - \frac{1}{2}, -\rangle)/\sqrt{2}$  by choosing  $\Delta\nu = (E_f - E_i)/h$  and  $\Omega_J t = \pi/4$  to apply a carrier  $\pi/2$  pulse. We then wait for a duration  $T$  and apply another  $\pi/2$  pulse with a variable phase relative to the first pulse. If the molecular state remains coherent through the second interaction, the probability to return to  $|\mathcal{T}_J\rangle$  varies sinusoidally with the relative phase. Fig. 5 shows this for  $J \in \{1, 2\}$  and  $T = 15$  ms. The fringes are suitable for metrology with sub-100 Hz resolution, although the systematic uncertainties have not yet been characterized at this level. The stability of the Raman beams

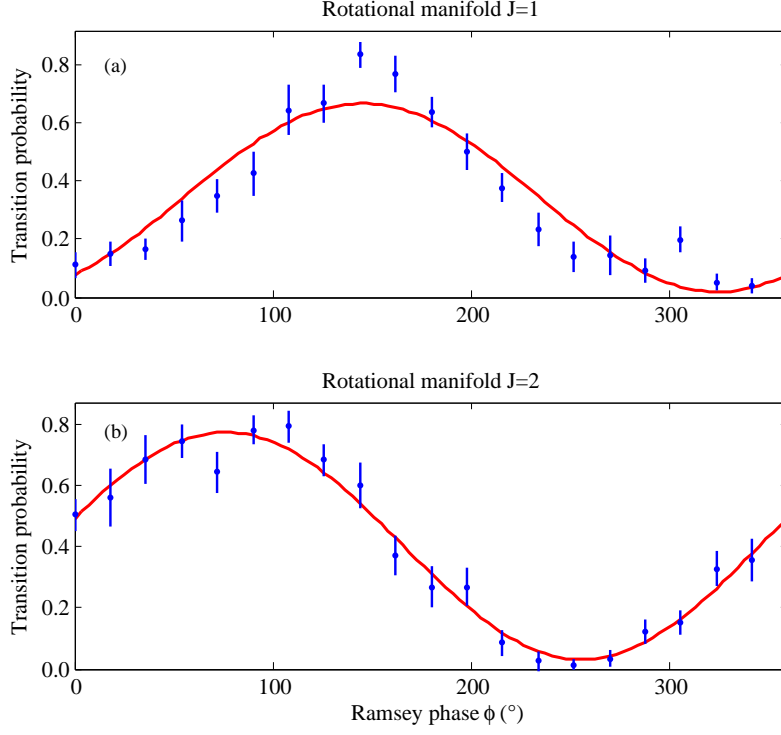


FIG. 5. Probability of making the transition  $|J, -J - \frac{1}{2}, -\rangle \rightarrow |\mathcal{T}_J\rangle$  after a Ramsey sequence with relative phase  $\phi$  between the two  $\pi/2$  pulses and a wait time of 15 ms for (a)  $J = 1$  and (b)  $J = 2$ . The red lines are fits to sinusoidal functions with periods of  $360^\circ$ .

could be further improved to better exploit the lifetime of the molecule in the rotational sublevels and achieve higher spectroscopic resolution with a longer Ramsey sequence.

In summary, we have demonstrated a method for preparation of pure states and non-destructive coherent spectroscopy of a trapped single molecular ion,  $^{40}\text{CaH}^+$ , based on elements of quantum-logic spectroscopy. All manipulations of the molecule are carried out with a single CW laser at 1051 nm that is far-detuned from all molecular transitions. The  $^{40}\text{CaH}^+$  molecular ion is a candidate for the detection of the variation in the proton-to-electron mass ratio [30]. The same laser and methods are readily applicable to precision spectroscopy and quantum state manipulation of a wide range of molecular species, including symmetric molecules such as  $\text{H}_2^+$  [31], and possibly molecules that have been identified as candidates to impose stringent limits on the electric dipole moment of the electron [32, 33], or the time dependence of fundamental constants [11]. In a next step, we will use a frequency comb as a second source of Raman pulses that can span the energy difference between rotational levels with different  $J$  [22, 23]. Rather than relying on blackbody radiation to

randomly populate a level with the desired  $J$ , this should allow us to coherently transfer the molecule from any pure state to the desired state on time scales much faster than the blackbody rates [22, 23]. We are optimistic that precise spectroscopic data on a multitude of molecular ions that may be relevant in astrophysics, stringent tests of fundamental theories as well as quantum information processing will be enabled by these techniques.

## ACKNOWLEDGEMENTS

We thank K. C. Cossel, Y. Wan, and D. J. Wineland for helpful comments on the manuscript. This work was supported by the U.S. Army Research Office and the NIST quantum information program. C. Kurz acknowledges support from the Alexander von Humboldt foundation. Contribution of National Institute of Standards and Technology, not subject to U.S. copyright.

## AUTHOR CONTRIBUTIONS

C.W.C. and D.L. conceived and designed the experiments. C.W.C. and C.K. developed components of the experimental apparatus and collected and analyzed data. C.W.C. and D.L. wrote the manuscript. D.B.H. and D.R.L. contributed to the development of experimental methods and pulse sequences. P.N.P. computed the molecular constants and level structure. All authors provided important suggestions for the experiments, discussed the results, and contributed to the editing of the manuscript.

## SUPPLEMENTARY INFORMATION

### Numerical Calculation of $\text{CaH}^+$ Properties

Calculating the properties of  $\text{CaH}^+$  requires an accurate potential energy curve to determine the equilibrium structure and rovibrational wave functions within the Born-Oppenheimer approximation. In a second step, properties (spin-rotation constant and g-factor) are computed as a function of the Ca-H internuclear distance  $r$ . The g-factor and spin-rotation constant for a given rovibrational state  $|Jv\rangle$  are computed as the expectation value with respect to the rovibrational wavefunction, for example  $g_{Jv} = \langle \Psi_{Jv}(r) | g(r) | \Psi_{Jv}(r) \rangle$ .

Calculations have been carried out with the program packages CFOUR [34] and MRCC [35] using coupled cluster (CC) methods. Different levels of coupled cluster theory are abbreviated according to the level of excitations in the exponential, e.g. CCSDTQ stands for coupled-cluster with single, double, triple and quadruple excitations. In CCSD(T), the contribution of triple excitations is determined from perturbation theory [36]. All calculations employ atom-centered Gaussian basis sets, the correlation-consistent polarized basis sets (cc-p) [37, 38], with valence-only (cc-pV) and core-valence (cc-pCV) correlation for Ca. The full basis set is specified by the number  $X$  of independent radial basis functions per correlated occupied orbital (XZ), for example cc-pCV5Z. All calculations are based on a closed-shell restricted Hartree-Fock reference. The frozen-core approximation has been used in coupled cluster calculations, with the 5 lowest (doubly occupied) orbitals in the frozen core. In the following we are not interested in total energies but only in the shape of the potential energy curve. As can be seen in Figure 6, the energy is well converged with respect to the cluster operator at the CCSDT level of theory. This is supported by comparison with CCSDTQ-calculations with deviations below 0.01 eV. In the range of the potential curve that is relevant for the vibrational ground state, CCSD(T) also agrees quantitatively with CCSDT. We therefore use CCSD(T) since it is accurate enough and most efficient. Increasing the basis set from cc-pCVQZ to cc-pCV5Z results in energy changes below 0.02 eV. The contribution of the diagonal Born-Oppenheimer correction (DBOC) and scalar-relativistic mass-velocity-1-electron-Darwin (MVD1) corrections are also on the order of 0.02 eV.

Vibrational wavefunctions are obtained by numerical solution of the Schrödinger equation using the full potential  $V_0(r)$  (energy of the electronic wavefunction as a function of Ca-H distance, using CCSD(T)) plus centrifugal potential:

$$V(r) = V_0(r) + \frac{\hbar^2 J(J+1)}{2\mu r^2}, \quad (7)$$

where  $\mu$  is the reduced mass and  $J$  is the rotational quantum number.

### **Hyperfine-coupling and g-factor from numerical electronic structure theory**

Spin-rotation constants and g-factors have been computed from coupled-cluster response theory using London atomic orbitals and rotational London atomic orbitals [39–42]. As

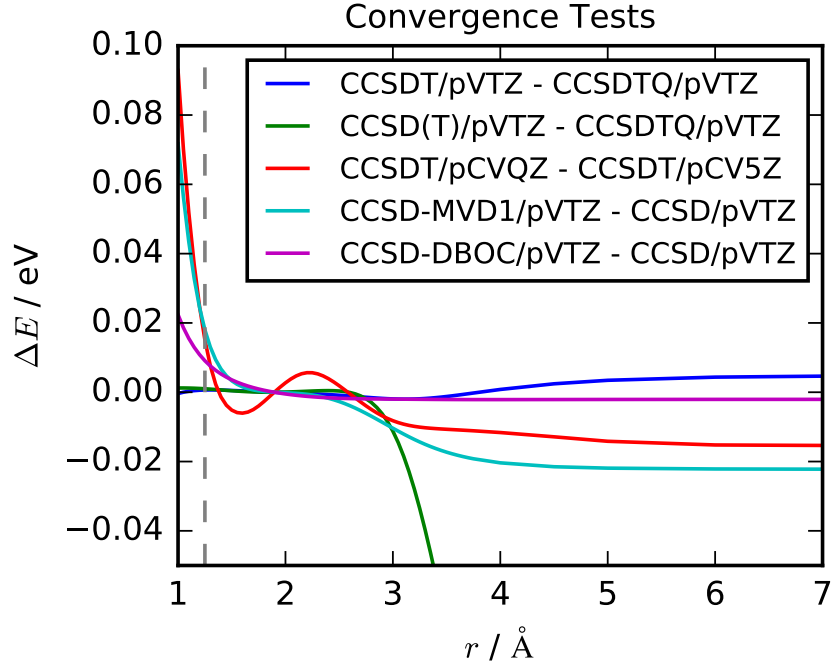


FIG. 6. Difference in energies obtained with different methods. All curves have been shifted to be zero at 1.896 Å. The grey dashed line is drawn at 1.25 Å which is the lower limit of a significant probability density at a high vibrational quantum number ( $v=10$ ). Basis sets are correlation-consistent basis sets (the cc has been omitted for clarity). MVD1 and DBOC donate mass-velocity-1-electron-Darwin and diagonal Born-Oppenheimer corrections.

has been found before, the calculations are not very sensitive to basis set size or core-correlation [39]. At the minimum of the potential energy curve, computed values for  $g$  and  $c_{IJ}$  deviate by about 0.1% comparing CCSDT and CCSD(T) and still by less than 0.5% comparing CCSDT and CCSD, demonstrating well-converged results with respect to the cluster operator (see Table I). Results obtained with the  $3\zeta$  basis set cc-pVTZ differ significantly from those obtained with larger basis sets, (13% for  $g$ ). The difference between the calculation with the largest and second-largest basis set (CCSD(T)/cc-pCV5Z and CCSD(T)/cc-pCVQZ) is 1.7% for  $g$  and 0.6% for  $c_{IJ}$ . In the literature, computed values based on a comparable level of theory deviate usually by less than 5 % from experimental values, and often the deviation is less than 1 % [39, 43–45]. Based on these results, we will use CCSD(T)/cc-pCV5Z to compute all properties and estimate the error of computed values of  $c_{IJ}$  and  $g$  to be  $\pm 5\%$ .

TABLE I. Numerical values of spin-rotation constant  $c_{IJ}$  and g-factor  $g$  at the approximate minimum of the potential energy curve  $r_0 = 1.896$  Å.

method	basis set	$g$	$c_{IJ}/\text{kHz}$
CCSD(T)	cc-pCVQZ	-1.38	8.47
CCSD(T)	cc-pCV5Z	-1.36	8.52
CCSD(T)	cc-pV5Z	-1.37	8.50
CCSD(T)	cc-pVTZ	-1.18	8.67
CCSDT	cc-pVTZ	-1.19	8.67
CCSD	cc-pVTZ	-1.18	8.71

Vibrationally averaged values are obtained using the vibrational wave-function as well as a polynomial interpolation of the property. Relativistic corrections to the spin-rotation constant from Thomas precession [46] have been included but are always small, being on the order of 10 Hz. The results are presented in Table II. The vibrational corrections are smaller for the g-factor, because  $g(r)$  is approximately linear in the relevant range of  $r$ . Since the vibrational ground state wavefunction is to a good approximation as symmetric around the equilibrium distance  $r_0$  as the harmonic approximation, the vibrational correction to any property that depends linearly on  $r$  nearly vanishes.

The behavior of the spin-rotation constant and g-factor as a function of the bond distance is shown in Figures 7 and 8.

### Magnetic sublevels of $\text{CaH}^+$

With the spin-rotation constant  $c_{IJ}$  and g-factor  $g$ , the structure of  $^{40}\text{CaH}^+$  magnetic sublevels in each  $J$ -manifold can be calculated by diagonalizing the Hamiltonian

$$H = -g\mu_N \mathbf{J} \cdot \mathbf{B} - g_I \mu_N \mathbf{I} \cdot \mathbf{B} - hc_{IJ} \mathbf{I} \cdot \mathbf{J}, \quad (8)$$

where  $g_I$  is the proton g-factor and  $\mu_N$  is the nuclear magneton. In our experiments, the external magnetic field defines the quantization axis,  $\mathbf{B} = B\hat{\mathbf{e}}_z$  and  $B \simeq 0.36$  mT. The molecule is neither in the Zeeman regime, where the mutual coupling of the spins is stronger than their coupling to the external field, nor the Paschen-Back regime where the spins



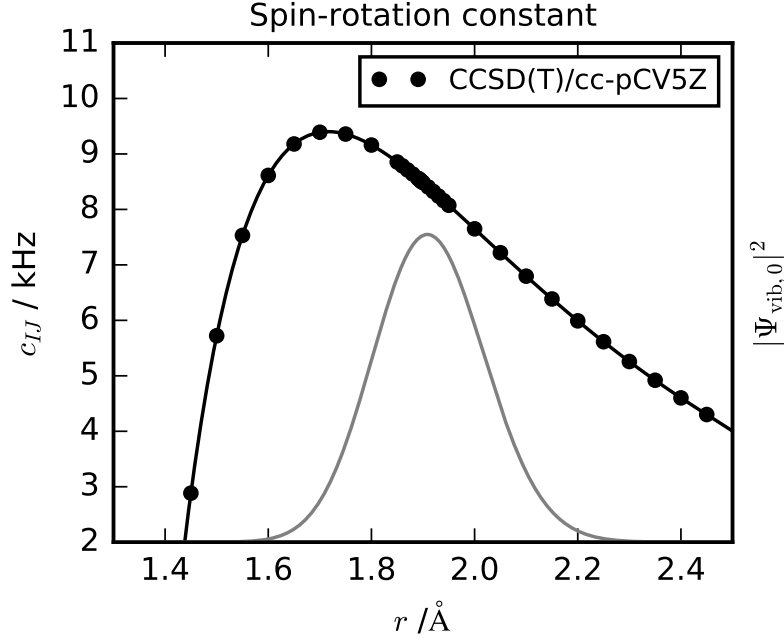


FIG. 7. Spin-rotation factor, fit with an 8th order polynomial. The squared vibrational wavefunction is shown in grey for  $J = 0$ .

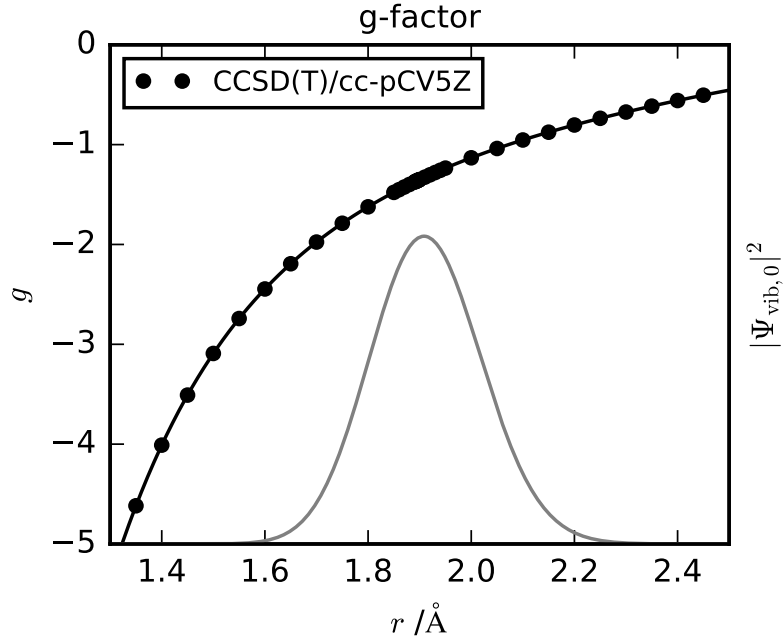


FIG. 8. g-factor, fit with an 8th-order polynomial. The squared vibrational wavefunction is shown in grey for  $J = 0$ .

TABLE II. Numerical values of spin-rotation constant  $c_{IJ}$  and g-factor  $g$  in the vibrational ground state  $v = 0$  and in the 15 lowest rotational states.

	$g$	$c_{IJ}/\text{kHz}$
$J = 0$	-1.35	8.27
$J = 1$	-1.35	8.26
$J = 2$	-1.35	8.26
$J = 3$	-1.34	8.26
$J = 4$	-1.34	8.26
$J = 5$	-1.34	8.25
$J = 6$	-1.34	8.25
$J = 7$	-1.34	8.24
$J = 8$	-1.33	8.24
$J = 9$	-1.33	8.23
$J = 10$	-1.33	8.22
$J = 11$	-1.32	8.21
$J = 12$	-1.32	8.20
$J = 13$	-1.31	8.19
$J = 14$	-1.31	8.18

tend to align with the magnetic field. Defining the eigenvalues of  $J_z + I_z$  as  $m = m_J + m_I$  and using the operator identity  $J_x I_x + J_y I_y = 1/2(J_+ I_- + J_- I_+)$  where  $J_\pm |J, m_J\rangle = \sqrt{(J \mp m_J)(J \pm m_J + 1)} |J, m_J \pm 1\rangle$  act as ladder operators, as long as  $|m| \leq J$  (and likewise  $I_\pm$ ), we can rewrite

$$H = (gJ_z + g_I I_z) \mu_N B - hc_{IJ} [J_z I_z + 1/2(J_+ I_- + J_- I_+)], \quad (9)$$

which shows that irrespective of the value of  $B$ ,  $m$  is a good quantum number, since all terms in  $H$  preserve  $m$ . For  $^{40}\text{CaH}^+$ , the nuclear spin of the proton is  $I = 1/2$  and the Hamiltonian is block-diagonal in the basis of product states  $|J, m_J\rangle |I, m_I\rangle$ . For the extreme cases  $m = \pm(J + 1/2)$ , the eigenstates of  $H$  are  $|J, \pm(J + 1/2), \pm\rangle = |J, \pm J\rangle |1/2, \pm 1/2\rangle$ , fully aligned product-states with energies  $E_{\pm(J+1/2), \pm} = \pm(gJ + g_I/2) \mu_N B \mp hc_{IJ} J/2$ . In all

other cases, the blocks have dimensions  $2 \times 2$  and the form

$$H_{J,m} = \begin{pmatrix} -\mu_N B[g(m - \frac{1}{2}) + \frac{g_I}{2}] - h\frac{c_{IJ}}{2}(m - \frac{1}{2}) & -h\frac{c_{IJ}}{2}\sqrt{(J + \frac{1}{2})^2 - m^2} \\ -h\frac{c_{IJ}}{2}\sqrt{(J + \frac{1}{2})^2 - m^2} & -\mu_N B[g(m + \frac{1}{2}) - \frac{g_I}{2}] + h\frac{c_{IJ}}{2}(m + \frac{1}{2}) \end{pmatrix}. \quad (10)$$

When diagonalizing such a block in analogy to the solution of the Breit-Rabi equation we get the eigenvectors

$$\begin{aligned} |J, m, +\rangle &= \sqrt{\frac{X - Y}{2X}} |J, m - 1/2\rangle |1/2, 1/2\rangle + \sqrt{\frac{X + Y}{2X}} |J, m + 1/2\rangle |1/2, -1/2\rangle \text{ and} \\ |J, m, -\rangle &= -\sqrt{\frac{X + Y}{2X}} |J, m - 1/2\rangle |1/2, 1/2\rangle + \sqrt{\frac{X - Y}{2X}} |J, m + 1/2\rangle |1/2, -1/2\rangle, \end{aligned} \quad (11)$$

with

$$\begin{aligned} X &= \frac{1}{2} \sqrt{h^2 c_{IJ}^2 [(J + \frac{1}{2})^2 - m^2] + [h c_{IJ} m - \mu_N B(g - g_I)]^2} \text{ and} \\ Y &= -\mu_N B(\frac{g}{2} - \frac{g_I}{p}) - m h \frac{c_{IJ}}{2}. \end{aligned} \quad (12)$$

The corresponding eigenvalues are

$$E_{m,\pm} = h \frac{c_{IJ}}{4} - \mu_N B g m \mp X. \quad (13)$$

The contribution from  $X$  can approximately cancel the other factors in  $E_{m,+}$ , leading to small and similar transition frequencies between states with different  $m$  in that manifold, while the  $m$ -dependent effects add up in  $E_{m,-}$  (shown for  $J = 1, 2$  in Fig. 2 of the main text). We take advantage of small frequency differences in both manifolds to pump several substates simultaneously, while using the most distinguishable transitions  $|J, -J+1/2, -\rangle \leftrightarrow |J, -J-1/2, -\rangle$  for state determination and spectroscopy (see also the sections on pumping and spectroscopy below). To simplify expressions containing the eigenstates in the main text, we use the abbreviation  $|\mathcal{J}\rangle$  as a shorthand for states with the set of quantum numbers  $|J, m, \xi\rangle$  with  $\xi \in \{+, -\}$ .

### Stimulated Raman transitions

Raman scattering on molecules usually involves a single light field at  $\omega_1$  that is far off-resonant from all intermediate excited states  $|f\rangle$ . Then the second, Stokes or Anti-Stokes photon at  $\omega_2$  is spontaneously emitted by the molecule as shown in Fig. 9 (a). In our

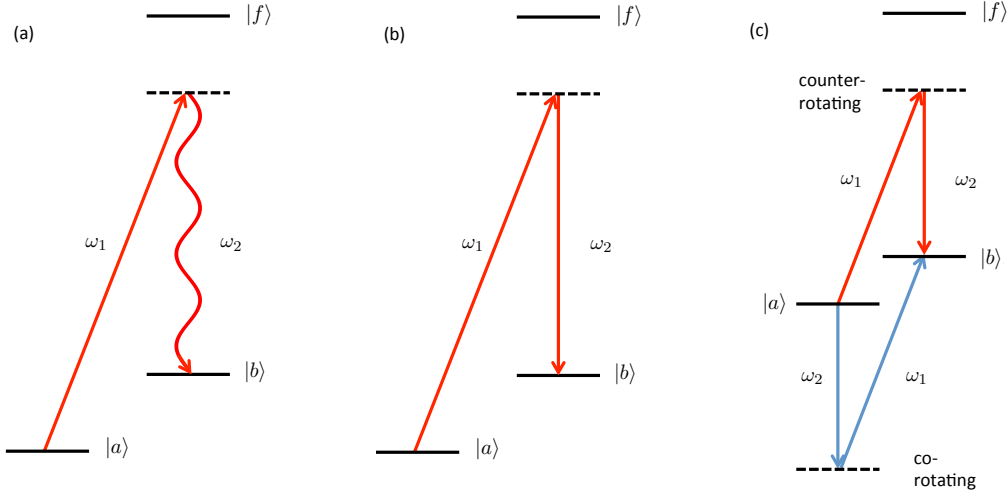


FIG. 9. Raman transitions: (a) Single field Raman transition, photon at  $\omega_2$  is spontaneously emitted. (b) Stimulated Raman transition, driven by two fields, photon at  $\omega_2$  is stimulated by the second driving field. (c) Order of absorption and emission and detuning of the coherence in the counter-rotating (red) and co-rotating (blue) cases.

experiments, we excite transitions from  $|a\rangle$  to  $|b\rangle$  where the second photon at  $\omega_2$  is stimulated by a second driving field at that frequency, as shown schematically in Fig. 9 (b). The second field greatly enhances the Raman scattering rate and leads to coherent transitions between  $|a\rangle$  and  $|b\rangle$ . The two driving light fields are characterized by ( $n = \{1, 2\}$ ) frequency  $\omega_n$ , field amplitude  $|\mathbf{E}_n|$  and polarization  $\hat{\mathbf{q}}^{(n)} = q_{-1}^{(n)}\sigma^- + q_0^{(n)}\pi + q_1^{(n)}\sigma^+$ ,  $|\hat{\mathbf{q}}^{(n)}|^2 = 1$ , where  $\pi$  is oriented along the quantizing magnetic field and  $\sigma^+$  ( $\sigma^-$ ) is circular polarization rotating clockwise (counter-clockwise) around that direction when viewed along the wavevector. The fields are far off-resonant from the smallest frequency difference between states of the molecule with the electrons in the ground state and those with electrons in excited states.

While each light field is very far detuned from resonance, we assume that the frequency difference  $\Delta\omega = (\omega_2 - \omega_1)$  is close to the frequency difference  $\omega_0 = 1/\hbar(E_b - E_a)$  of the initial molecular state  $|a\rangle$  and a final state  $|b\rangle$ . Then, the Raman-Rabi-frequency  $\Omega_{ab}$  for a stimulated Raman transition can be approximated in perturbation theory as

$$\Omega_{ab} = \frac{1}{4\hbar^2} \sum_f \frac{\langle b|e \mathbf{r} \cdot \mathbf{E}_2|f\rangle \langle f|e \mathbf{r} \cdot \mathbf{E}_1|a\rangle}{\omega_{af} - \omega_1} + \frac{\langle b|e \mathbf{r} \cdot \mathbf{E}_1|f\rangle \langle f|e \mathbf{r} \cdot \mathbf{E}_2|a\rangle}{\omega_{af} + \omega_2}, \quad (14)$$

where  $e$  is the charge of the electron,  $\mathbf{r}$  its position and  $\omega_{af} = 1/\hbar(E_f - E_a)$  is the frequency

difference between the initial state  $|a\rangle$  and an intermediate state  $|f\rangle$ . The term in the sum with denominator  $\omega_{af} - \omega_1$  is due to terms rotating at the difference frequency between the first light field and the energy difference of initial and intermediate state. In most textbook discussions, the difference is assumed to be much smaller than the sum  $\omega_{af} + \omega_2$  that appears in the denominator of the other term. In these cases, terms in the perturbation expansion co-rotating at this sum are neglected with respect to the counter-rotating terms at the difference frequency in what is called the rotating wave approximation. However, in our experiments, the light fields are detuned so far that the ratio of difference to sum is approximately 1:2.3 for laser light near 1051 nm and estimating the energy difference of the ground and first excited electronic levels according to [29]. Therefore, we cannot necessarily neglect the co-rotating terms. The difference in the processes is illustrated in Fig. 9 (c): For the counter-rotating terms (red arrows), the photon at  $\omega_1$  is absorbed to set up a coherence in the molecule that rotates at  $\omega_{af} - \omega_1$ , then a photon at  $\omega_2$  is stimulated. In the co-rotating term (blue arrows), the photon at  $\omega_2$  is stimulated first, setting up a coherence at the larger detuning  $\omega_{af} + \omega_2$ , then  $\omega_1$  is absorbed, leading to the same resonance condition and selection rules as in the counter-rotating term.

In our experiments, initial and final states are in the electronic ground state,  $|1^1\Sigma\rangle$  in the notation of [29], vibrational ground state,  $v = 0$ , and a particular manifold of the rotation characterized by quantum number  $J$ . To determine the Raman-Rabi-rate, we need to evaluate dipole matrix elements of the form

$$\langle f|e \mathbf{r} \cdot \mathbf{E}|s\rangle = e|\mathbf{E}|\langle \Psi_{f,v}(r)|r|1^1\Sigma, v=0\rangle\langle \Phi_f(\theta, \phi)|\hat{\mathbf{r}} \cdot \hat{\mathbf{q}}|\Phi_s(\theta, \phi)\rangle, \quad (15)$$

where  $s \in \{a, b\}$ . On the right-hand side we have factored the molecular wave functions into two parts. The radial part of the excited state electronic wave-function  $\Psi_{f,v}(r)$  only depends on the inter-nuclear distance  $r = |\mathbf{r}|$  and vibrational quantum number  $v$ . The angular part of the wavefunction  $\Phi_s(\theta, \phi)$  only depends on the two angle coordinates  $\theta$  and  $\phi$ . Such a separation of variables can be justified, for example, within the Born-Oppenheimer approximation. Here, we only consider the lowest excited electronic state  $|2^1\Sigma\rangle$  and neglect the differences in  $\omega_{af}$  due to the rotational and vibrational states,  $\omega_{af} \simeq 1/\hbar(E_{2^1\Sigma} - E_{1^1\Sigma}) \equiv$

$\bar{\omega}$ . Under these assumptions we can rewrite Eq.(14) as

$$\begin{aligned}
\Omega_{ab} &= \mathcal{E}(S_- + S_+) \\
\mathcal{E} &= \frac{e^2 |\mathbf{E}_1| |\mathbf{E}_2|}{4\hbar^2 (\bar{\omega} - \omega_1)} \sum_{v'} |\langle \Psi_{2^1\Sigma, v'} | r | \Psi_{1^1\Sigma, 0} \rangle|^2, \\
S_- &= \sum_f \langle \Phi_b | \hat{\mathbf{r}} \cdot \hat{\mathbf{q}}^{(2)} | \Phi_f \rangle \langle \Phi_f | \hat{\mathbf{r}} \cdot \hat{\mathbf{q}}^{(1)} | \Phi_a \rangle \\
S_+ &= \frac{\bar{\omega} - \omega_1}{\bar{\omega} + \omega_1} \sum_f \langle \Phi_b | \hat{\mathbf{r}} \cdot \hat{\mathbf{q}}^{(1)} | \Phi_f \rangle \langle \Phi_f | \hat{\mathbf{r}} \cdot \hat{\mathbf{q}}^{(2)} | \Phi_a \rangle,
\end{aligned} \tag{16}$$

where we have also neglected the small frequency differences between the driving fields  $\omega_1 \simeq \omega_2$  in the denominators. Under these approximations,  $\mathcal{E}$  is a prefactor that is the same for all transitions considered here and is proportional to the sum over the squares of all Franck-Condon factors of vibrational states bound in the well of the first excited electronic state.

The position operator  $\mathbf{r}$  couples eigenstates of the rotational angular momentum  $|J, m_J\rangle$  and has no effect on the eigenstates of the proton nuclear spin  $|I, m_I\rangle$ . Therefore, it is convenient to use the product basis  $|J, m_J\rangle |I, m_I\rangle$  with the nuclear spin  $I$  fixed. In  $^{40}\text{CaH}^+$ , the nuclear spin  $I = 1/2$  is that of the proton. The sum over the intermediate states  $\Phi_f$  in  $S_-$  is

$$S_- = \sum_{J, m_J, m_I} \langle \Phi_b | \hat{\mathbf{r}} \cdot \hat{\mathbf{q}}^{(2)} | J, m_J \rangle | I, m_I \rangle \langle J, m_J | \langle I, m_I | \hat{\mathbf{r}} \cdot \hat{\mathbf{q}}^{(1)} | \Phi_a \rangle \tag{17}$$

The sum of angular momenta in the z-direction  $m_s = m_J + m_I$  remains a good quantum number for all values of the magnetic field  $\mathbf{B} = B\hat{\mathbf{e}}_z$ . This implies that we can write the eigenstates as

$$|\Phi_s\rangle = \sum_{m_I} c_{m_I}^{(s)} |J_s, m_s - m_I, 1/2, m_I\rangle, \quad s \in \{a, b\}, \tag{18}$$

where  $c_{m_I}^{(s)}$  are the coefficients of the eigenstates derived in Eq.(11). Inserting Eq.(18) into Eq.(17) yields

$$S_- = \sum_{J, m_J, m_I} c_{m_I}^{(b)} c_{m_I}^{(a)} \langle J_b, m_b - m_I | \hat{\mathbf{r}} \cdot \hat{\mathbf{q}}^{(2)} | J, m_J \rangle \langle J, m_J | \hat{\mathbf{r}} \cdot \hat{\mathbf{q}}^{(1)} | J_a, m_a - m_I \rangle. \tag{19}$$

We can express  $\hat{\mathbf{r}}$  as a vector in the spherical basis to write out the scalar product and use the Wigner-Eckart theorem to determine the matrix element for photon absorption from a

field with polarization  $\hat{\mathbf{q}}$ :

$$\langle J, m | \hat{\mathbf{r}} \cdot \hat{\mathbf{q}} | J', m' \rangle = \sqrt{\text{Max}(J, J')} (J - J') \sum_{k=-1}^1 \hat{q}_k (-1)^{k+J-m} \begin{pmatrix} J & 1 & J' \\ -m & k & m' \end{pmatrix}, \quad (20)$$

where the 2x3 array in brackets at the end is a Wigner 3J-symbol. The right hand side implies the usual dipole selection rules which reduce the number of excited states that need to be considered in the Raman Rabi-frequency as well as the final states that can have a non-zero coupling to  $|\Phi_a\rangle$ . In particular,  $\Delta J = J_b - J_a = 0, \pm 2$  and  $\Delta m = m_b - m_a = 0, \pm 1, \pm 2$ . Restricting the sums with the selection rules and setting  $m_{J_a} = m_a - m_I$ , we get

$$\begin{aligned} S_- = & \sum_{m_I=-1/2}^{1/2} \sum_{k_1, k_2=-1}^1 c_{m_I}^{(b)} c_{m_I}^{(a)} \left[ \langle J_a - 1, m_{J_a} + k_1 | \hat{r}_{k_2} q_{k_2}^{(2)} | J_b, m_{J_a} + k_1 - k_2 \rangle \times \right. \\ & \langle J_a - 1, m_{J_a} + k_1 | \hat{r}_{k_1} q_{k_1}^{(1)} | J_a, m_{J_a} \rangle + \\ & \langle J_a + 1, m_{J_a} + k_1 | \hat{r}_{k_2} q_{k_2}^{(2)} | J_b, m_{J_a} + k_1 - k_2 \rangle \times \\ & \left. \langle J_a + 1, m_{J_a} + k_1 | \hat{r}_{k_1} q_{k_1}^{(1)} | J_a, m_{J_a} \rangle \right], \quad (21) \end{aligned}$$

with the matrix elements all written in the form where the photon is absorbed to be compatible with Eq.(20). The expressions for  $S_+$  are calculated in the same way, but the available intermediate states change since the photon from field  $\mathbf{E}_2$  and its angular momentum is absorbed first in those terms.

AC-Stark shifts arise due to Raman transitions with  $|a\rangle = |b\rangle$  and amount to an energy shift of state  $|a\rangle$  by  $\Delta E_{AC} = \hbar \Omega_{aa}$ . If the two driving fields have different frequencies and/or polarizations, both photons contributing to a Raman transition need to come from the same field to conserve energy and angular momentum. For two fields with polarizations  $\hat{\mathbf{q}}^{(1)}, \hat{\mathbf{q}}^{(2)}$  and setting  $J_a = J$ ,  $m_a = m$  and  $c_{m_I}^{(a)} = c_{m_I}$  we can simplify Eq.(16) to

$$\begin{aligned} \Delta E_{AC} = (\mathcal{E}_1 + \mathcal{E}_2) S_- \frac{2\bar{\omega}}{\bar{\omega} - \omega_1} = \frac{2\bar{\omega}}{\bar{\omega} - \omega_1} \sum_{n=1}^2 \mathcal{E}_n \sum_{m_I=-1/2}^{1/2} |c_{m_I}|^2 \times \\ \left[ \frac{(m + m_I)^2 (3|q_0^{(n)}|^2 - 1)}{3 - 4J(J+1)} + \frac{1 - J(J+1)(|q_0^{(n)}|^2 + 1)}{3 - 4J(J+1)} \right]. \quad (22) \end{aligned}$$

The AC-Stark shift can be made state independent in several ways. For example, one can choose  $|q_0^{(n)}|^2 = 1/3$  to yield

$$\Delta E_{AC} = (\mathcal{E}_1 + \mathcal{E}_2) \frac{2\bar{\omega}}{3(\bar{\omega} - \omega_1)}. \quad (23)$$

In our experiments we chose the polarizations of one field, described by  $\mathcal{E}_1$  to be linear ( $|q_0^{(1)}|^2 = 1$ ) and the other field with circular polarization ( $|q_0^{(2)}|^2 = 0$ ) and having twice the intensity of the linearly polarized field  $\mathcal{E}_2 = 2 \mathcal{E}_1$ . Then the AC-Stark shift is also state independent,

$$\Delta E_{AC} = \mathcal{E}_1 \frac{2\bar{\omega}}{(\bar{\omega} - \omega_1)}. \quad (24)$$

In both cases, the AC-Stark shifts produce a global shift of all energy levels under the assumption of large laser detuning. The global shift will not affect the eigenstates of the Hamiltonian, therefore, the eigenstates are not changed when the light fields are turned on and off and the observed transition frequencies, that are proportional to energy differences, are not altered by these AC-Stark shifts. The validity of this approximation can be estimated by looking at the relative difference between energy denominators in Eq.(14). The contributing intermediate states are  $J + 1$  and  $J - 1$ , therefore, the energy differs by  $\Delta E = \hbar R(2 + 4J) \leq 26 \hbar R$  for  $J \leq 6$ ,  $\Delta E \simeq h \times 3.74$  THz for  $J = 6$ . The energy difference between the ground and the vibrational ground state in the first excited electronic state is roughly  $h \times 430.8$  THz [29]. Therefore, all energy denominators deviate by less than 1%.

In the experiment, the intensities of the  $\sigma$  and  $\pi$  beams are calibrated with the AC Stark shifts on the  $|S, m_F = -1/2\rangle \leftrightarrow |D, m_F = -5/2\rangle$  transition. During the calibration, the ion order is switched such that the  $^{40}\text{Ca}^+$  ion is where the  $^{40}\text{CaH}^+$  would be in the spectroscopy experiments. The power in both beams is actively controlled to yield stable Stark shifts during experiments. AC Stark shifts of 200 kHz and 130 kHz for the  $\sigma^-$ - and  $\pi$ -polarized beams are used in the sideband pulses. We experimentally find minimal shifts in the transition frequencies inferred from sideband and carrier measurements at the ratio of 2:1.3 for the Stark shifts on  $^{40}\text{Ca}^+$ .

### Trap parameters

The ions are trapped in a linear Paul trap consisting of two wafers with segmented DC electrodes. Some details about the trap construction can be found in [47]. The secular frequencies for single  $^{40}\text{Ca}^+$  are  $\{\nu_x, \nu_y, \nu_z\} = \{4.567, 7.546, 3.000\}$  MHz. In the experiment, the order of the two-ion crystal is monitored and maintained the same throughout to improve the consistency of laser beam illumination and micro-motion compensation during the



experiments.

### Sympathetic ground-state cooling

Ground-state cooling before the spectroscopy experiments is achieved by an initial stage of Doppler cooling with the 397 nm  $\pi$  beam (blue arrow perpendicular to the magnetic field in Fig. 1 of the main text), followed by EIT cooling with the 397 nm  $\pi$  and  $\sigma$  beams (blue arrow parallel with the magnetic field) [48], and resolved sideband cooling of the in-phase (IP) and out-of-phase (OOP) modes in the  $z$  direction and the lower frequency ( $\sim 3.4$  MHz) out-of-phase rocking (ROC) mode in the  $x$  direction with the 729 nm beam (red arrow perpendicular to the B field). We use the  $z$  OOP mode with low ( $< 1$  quanta/100 ms) heating rate for quantum-logic readout with low false-positive error rates. The  $x$  ROC mode is cooled to the ground state to avoid adverse effects from the parametric coupling between that mode and the readout mode [49]. The  $D_{5/2}$  and  $D_{3/2}$  states are repumped by the 854 and 866 nm beams (pink arrows perpendicular to the B field in Fig. 1 of the main text).

### Pumping of molecular states

The room temperature environment in our experiment equilibrates the  $^{40}\text{CaH}^+$  population with the background blackbody radiation (BBR) such that it is in the electronic and vibrational ground state with very high probability ( $> 99\%$ ). The populations in the rotational levels are thermally distributed. For  $^{40}\text{CaH}^+$  in  $B \sim 0.36$  mT, the frequencies of most  $|J, m, \xi\rangle \rightarrow |J, m - 1, \xi\rangle$ ,  $\xi \in \{+, -\}$ , transitions fall into narrow regions around -2 and -6 kHz, respectively. Pumping of the molecular population can be achieved by driving the OOP blue sideband (BSB) of those transitions followed by OOP mode sideband cooling pulses on  $^{40}\text{Ca}^+$  [21]. The population is pumped toward the  $-(J \pm \frac{1}{2})$  ends by ensuring that the frequency of the 1051 nm  $\sigma^-$  beam is higher than that of the  $\pi$  beam by the OOP mode frequency,  $\nu_t \sim 5.164$  MHz, minus the frequency of the transition with  $\Delta m = -1$  to be driven. Pumping of the spectroscopically resolved transitions  $|J, -J + 1/2, +\rangle \leftrightarrow |J, -J + 3/2, -\rangle$  and  $|J, -J - 1/2, -\rangle \leftrightarrow |J, -J + 1/2, -\rangle$  is interspersed to accumulate all of the molecular population in the states  $|J, -J + 1/2, -\rangle$  (see Fig. 2 of the main text for  $J=1,2$ ).

The pumping pulses from the 1051 nm beams do not change the rotation quantum number  $J$  and thus maintain the equilibrium population in each  $J$  manifold dictated by the background blackbody radiation.

### **Projective purification of imperfect $\text{Ca}^+$ state preparation**

To achieve a low false-positive error rate in the experiment, imperfect  $^{40}\text{Ca}^+$  state preparation and ground-state cooling are purified by exploiting the high detection fidelity in  $^{40}\text{Ca}^+$  state determination. With fluorescence count rates at  $> 2 \times 10^5$  and  $< 4 \times 10^3$  counts per second when the  $^{40}\text{Ca}^+$  is in the  $|S\rangle$  and  $|D\rangle$  states, respectively, the detection fidelity can be  $> 0.9999$  [28]. The target state,  $|D\rangle|0\rangle$ , is prepared via two purification stages. First, after ground-state cooling, a carrier  $\pi$  pulse converts  $|S\rangle$  to  $|D\rangle$ . If the  $^{40}\text{Ca}^+$  is found to be bright in the subsequent detection pulse, the state preparation starts over. Otherwise, the second purification stage follows, where a BSB  $\pi$  pulse converts  $|D\rangle|1\rangle$  to  $|S\rangle|0\rangle$  but leaves  $|D\rangle|0\rangle$  unaffected. The subsequent detection pulse would signal most of the population not in  $|0\rangle$  with a bright outcome and state preparation would start again from the beginning. The two dark outcomes from the first two purification stages leave the population mostly in  $|D\rangle|0\rangle$  and the ions are ready for a spectroscopy experiment. The spectroscopy pulse on the molecule will deposit a quantum of motion in the OOP mode if successful or leave that mode in the ground state otherwise. This is followed by a BSB  $\pi$  pulse on the atomic ion, transforming  $|D\rangle|1\rangle$  to  $|S\rangle|0\rangle$ . A bright outcome in the final detection pulse signals creation of a phonon in the OOP mode due to the spectroscopy experiments. A flow chart for the sequence is shown in Fig. 10. Using the purifying preparation sequence, false positive errors can be reduced to  $\sim 0.5\%$  for spectroscopy experiments shorter than 1.5 ms. A similar sequence is also implemented when the  $|D\rangle|1\rangle$  state is prepared for the spectroscopy experiments. Heating increases the false-positive error rates with increasing duration of the spectroscopy experiments.

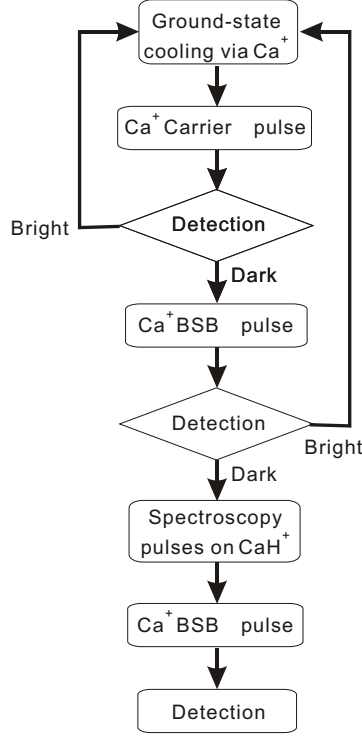


FIG. 10. Flow chart of the purification stages.

### Experimental sequences for repetitive projective state preparation, Rabi spectroscopy, and Ramsey fringes

Coherent spectra, Rabi flopping, and Ramsey fringes are obtained by repeating experimental sequences consisting of projective state preparation, molecular spectroscopy pulses, and state detection. The experiment control system attempts to keep track of the current state of the molecule. In the preparation stage, pumping is applied periodically if the rotational state of the molecule is unknown. Between pumping, projective state preparation for various  $J$ -manifold is attempted by applying Raman sideband  $\pi$  pulses to drive the  $|\mathcal{T}_J\rangle|0\rangle \rightarrow |J, -J - 1/2, -\rangle|1\rangle$  transition and detecting the results. A positive event prompts subsequent projective state preparation attempts for the same  $J$ . We require at least two consecutive positive events signaling the transitions  $|\mathcal{T}_J\rangle|0\rangle \leftrightarrow |J, -J - \frac{1}{2}, -\rangle|1\rangle$  before the experiment control signals the successful preparation of the molecule in  $|J, -J - \frac{1}{2}, -\rangle$ . The repetitive projection filters the false-positive events and thus achieves higher fidelity in projective state preparation. If four consecutive negative events are registered, the experiment control determines that the molecule is not in the corresponding manifold and switches to

attempt state preparation on a target transition with different  $J$ . After the projective state preparation is heralded, the state of the  $^{40}\text{Ca}^+$  ion and the motional mode are prepared in  $|D\rangle|0\rangle$ . For the coherent spectra and Rabi flopping, we apply the carrier pulse with variable  $\Delta\nu$  and pulse duration, respectively, to drive the  $|J, -J - \frac{1}{2}, -\rangle \leftrightarrow |\mathcal{T}_J\rangle$  transition. For the Ramsey fringes, two carrier  $\pi/2$  pulses on the transition are applied, separated by a delay of duration  $T$ , with variable relative phase between the two pulses. We then detect whether the molecule has made the transition to  $|\mathcal{T}_J\rangle = |J, -J + \frac{1}{2}, -\rangle$ . A sideband  $\pi$  pulse on the molecular  $|\mathcal{T}_J\rangle|0\rangle \leftrightarrow |J, -J - \frac{1}{2}, -\rangle|1\rangle$  transition followed by a sideband pulse driving the  $|D\rangle|1\rangle \rightarrow |S\rangle|0\rangle$  transition in  $^{40}\text{Ca}^+$  are applied. The state detection ends with a fluorescence detection with the outcome  $|S\rangle$  signaling a positive molecular transition event. By repeating the sequence we can measure the transition probabilities.

### Comparison of calculated and experimental molecular transition parameters

We presented spectroscopy experiments on the motional sidebands of the  $|\mathcal{T}_J\rangle \leftrightarrow |J, -J - 1/2, -\rangle$  transitions (see Fig. 3 in the main text), as well as carrier transitions (see Fig. 4, main text). Determination of energy differences based on the carrier transitions should reduce systematic uncertainties as compared with sideband transitions for two reasons: (i) Drifts of the secular frequency over time does not contribute to the uncertainties in the measured resonance frequencies. (ii) For a given Rabi rate, the light intensity on a carrier transition can be reduced by a factor of  $\eta$ , the Lamb-Dicke parameter, compared with a sideband transition. This significantly reduces the differential AC Stark shift induced by the probe laser beams. Table III lists the experimental carrier transition frequencies for the rotational manifolds  $J = 1, 2, \dots, 6$  at  $1/8$  of the light intensity used for the sideband transitions shown in Fig. 3 in the main text, as well as the predictions from our theoretical model. Experimental errors are purely statistical and theoretical uncertainties are based on the assumption that uncertainties in the parameters  $c_{IJ}$  and  $g$  add like random and independent variables. While the proximity of the experimental frequencies to the calculated frequencies supports our identification of the transitions, we are unable to perform a quantitative comparison, which would require careful characterization of systematic uncertainties in the experiment and of correlations between the theoretical uncertainties.

We also compared the experimentally determined Rabi rates from the Rabi flopping

TABLE III. Comparison between experiment and theory for spectroscopy on the carrier transitions. Listed are the observed and calculated center frequencies of the transitions  $|\mathcal{T}_J\rangle \leftrightarrow |J, -J-1/2, -\rangle$ . Experimental uncertainties are statistical, indicating the 68 % confidence interval. Theoretical values are computed using the spin-rotation constants and g factors from Table II, the magnetic-field value  $B = 0.357$  mT and taking into account off-resonant coupling of the levels  $|\mathcal{T}_J\rangle$  and  $|J, -J-1/2, -\rangle$  to other magnetic sublevels when driven by the Raman beams. Theoretical uncertainties are based on a 5 % estimate for the relative uncertainties of the constants, using Gaussian error propagation. It should be noted that, unlike in the case of statistical uncertainties, the theoretical uncertainties might be correlated and Gaussian error propagation is hence only an approximation.

$J$	Experiment (kHz)	Theory (kHz)
1	10.94(14)	10.73(44)
2	13.55(8)	13.51(80)
3	18.42(10)	18.90(1.27)
4	24.90(15)	25.56(1.75)
5	31.79(7)	32.85(2.20)
6	39.51(5)	40.54(2.64)

curves in Fig. 4 in the main text with theory. For the probed transitions in the  $J = 1$  and  $J = 2$  manifolds, we find the Rabi rates  $\Omega_{J=1} = 2\pi \times 2.078(14)$  kHz and  $\Omega_{J=2} = 2\pi \times 1.804(12)$  kHz, respectively (uncertainties are statistical). The ratio of the two is 1.152(11), in reasonable agreement with the value 1.132 predicted by Eqs. (16) and (21).

- 
- [1] Cornell, E. A., and Wieman, C. E., Nobel Lecture: Bose-Einstein condensation in a dilute gas, the first 70 years and some recent experiments, Rev. Mod. Phys. 74, 875 (2002).
  - [2] Ketterle, W., Nobel lecture: When atoms behave as waves: Bose-Einstein condensation and the atom laser, Rev. Mod. Phys. 74, 1131 (2002).

- [3] DeMarco, B. and Jin, D. S., Onset of Fermi degeneracy in a trapped atomic gas, *Science* 285, 1703 (1999).
- [4] O'Hara, K. M., Granade, S. R., Gehm, M. E., Savard, T. A., Bali, S., Freed, C., and Thomas, J. E., Ultrastable CO<sub>2</sub> laser trapping of lithium Fermions, *Phys. Rev. Lett.* 82, 4204 (1999).
- [5] Mitchell, T.B., Bollinger, J. J., Dubin, D. H. E., Huang, X.-P., Itano, W. M., Baughman, R. H. , Direct observations of structural phase transitions in planar crystallized ion plasmas, *Science* 282, 1290 (1998).
- [6] Kitching, J., Knappe, S., and Donley, E. A., Atomic sensors - a review, *IEEE Sens. Jou.* 11, 1749 (2011) and references therein.
- [7] Ludlow, A. D., Boyd, M. M., Ye, J., Peik, E., and Schmidt, P. O., Optical atomic clocks, *Rev. Mod. Phys.* 87, 637 (2015).
- [8] Carr, L. D., DeMille, D., Krems, R. V., and Ye, J., Cold and ultracold molecules: science, technology and applications, *New J. Phys.* 11, 055049 (2009).
- [9] DeMille, D., Diatomic molecules, a window onto fundamental physics, *Phys. Today* 68, 34 (2015)
- [10] Koelemeij, J., Roth, B., Wicht, A., Ernsting, I., and Schiller, S., Vibrational Spectroscopy of HD<sup>+</sup> with 2-ppb Accuracy. *Phys. Rev. Lett.* 98 (2007).
- [11] Schiller, S., and Korobov, V., Tests of time independence of the electron and nuclear masses with ultracold molecules, *Phys. Rev. A*, 71, 032505 (2005)
- [12] Flambaum, V., and Kozlov, M., Enhanced sensitivity to the time variation of the fine-Structure constant and  $m_p/m_e$  in diatomic molecules, *Phys. Rev. Lett.* 99 150801 (2007).
- [13] Pupillo, G., Micheli, A., Büchler, H.-P., and Zoller, P. in *Cold Molecules: Theory, Experiment, Applications* (eds Krems, R., Friedrich, B. and Stwalley, W. C.) Ch. 12 (CRC Press 2009)
- [14] DeMille, D., Quantum computation with trapped polar molecules, *Phys. Rev. Lett.* 88, 067901 (2002).
- [15] Ospelkaus, S., Ni, K.-K., Quéméner, G., Neyenhuis, B., Wang, D., de Miranda, M. H. G., Bohn, J. L., Ye, J., and Jin, D. S., Controlling the hyperfine state of rovibronic ground-state polar molecules, *Phys. Rev. Lett.*, 104, 030402 (2010).
- [16] Will, S. A., Park, J. W., Yan, Z. Z., Loh, H., and Zwierlein, M., Coherent microwave control of ultracold Na<sup>23</sup>K<sup>40</sup> molecules, *Phys. Rev. Lett.* 116, 225306 (2016).
- [17] Lien, C.-Y., Seck, C. M., Lin, Y.-W., Nguyen, J.H.V., Tabor, D. A. and Odom, B. C., Broad-

- band optical cooling of molecular rotors from room temperature to the ground state. *Nature Commun.* 5, 4783 (2014).
- [18] Shuman, E. S., Barry, J. F., and Demille, D., Laser cooling of a diatomic molecule, *Nature* 467, 820 (2010).
  - [19] Barrett, M. D., DeMarco, B., Schaetz, T., Meyer, V., Leibfried, D., Britton, J., Chiaverini, J., Itano, W. M., Jelenkovi, B., Jost, J. D., Langer, C., Rosenband, T., and Wineland, D. J., Sympathetic cooling of  $^9\text{Be}^+$  and  $^{24}\text{Mg}^+$  for quantum logic, *Phys. Rev. A* 68, 042302 (2003).
  - [20] Wolf, F., Wan, Y., Heip, J. C., Gebert, F., Shi, C., and Schmidt, P. O., Non-destructive state detection for quantum logic spectroscopy of molecular ions, *Nature* 530, 457 (2016).
  - [21] Schmidt, P.O., Rosenband, T., Langer, C., Itano, W. M., Bergquist, J. C., and Wineland, D. J., Spectroscopy using quantum logic, *Science* 309, 749 (2005).
  - [22] Leibfried, D., Quantum state preparation and control of single molecular ions, *New J. Phys.* 14, 023029 (2012).
  - [23] Ding, S. and Matsukevich, D. N., Quantum logic for the control and manipulation of molecular ions using a frequency comb, *New J. Phys.* 14, 023028 (2012).
  - [24] Rungango, R., Goeters, J. E., Dixon, T. H., Gray, J. M., Khanyile, N. B., Shu, G., Clark, R. J., and Brown, K. R., Sympathetic cooling of molecular ion motion to the ground state, *New J. Phys.* 17 035009 (2015).
  - [25] Kimura, N., Okada, K., Takayanagi, T., Wada, M., Ohtani, S., and Schuessler, H. A., Sympathetic crystallization of  $\text{CaH}^+$  produced by a laser-induced reaction, *Phys. Rev. A* 83 033422 (2011).
  - [26] Roos, Ch., Zeiger, Th., Rohde, H., Ngerl, H. C., Eschner, J., Leibfried, D., Schmidt-Kaler, F., and Blatt, R., Quantum state engineering on an optical transition and decoherence in a Paul trap, *Phys. Rev. Lett.* 83 4713 (1999).
  - [27] Leibfried, D., Blatt, R., Monroe, C., and Wineland, D., Quantum dynamics of single trapped ions, *Rev. Mod. Phys.* 75, 281(2003).
  - [28] Myerson, A. H., Szwer, D. J., Webster, S. C., Allcock, D.T., Curtis, M. J., Imreh, G., Sherman, J. A., Stacey, D. N., Steane, A.M., Lucas, D. M., High-fidelity readout of trapped-ion qubits, *Phys. Rev. Lett.* 100, 200502 (2008).
  - [29] Abe, M., Moriwaki, Y., Hada, M., and Kajita, M., Ab initio study on potential energy curves of electronic ground and excited states of  $^{40}\text{CaH}^+$  molecule, *Chem. Phys. Lett.* 521, 31 (2012)

- [30] Kajita, M. and Moriwaki, Y., Proposed detection of variation in  $m_p/m_e$  using a vibrational transition frequency of a  $\text{CaH}^+$  ion, *J. Phys. B* 42 154022 (2009).
- [31] Ubachs, W., Koelemeij, J.C.J., Eikema, K.S.E., Salumbides, E.J., Physics beyond the Standard Model from hydrogen spectroscopy, *J. Mol. Spec.* 320, 1 (2016).
- [32] Meyer, E. R., Bohn, John L., and Deskevich, Michael P., Candidate molecular ions for an electron electric dipole moment experiment, *Phys. Rev. A* 73, 062108 (2006).
- [33] Loh, H., Cossel, K. C., Grau, M. C., Ni, K.-K., Meyer, E. R., Bohn, J. L., Ye, J., Cornell, E. A., Precision spectroscopy of polarized molecules in an ion trap, *Science*, 342, 1220 (2013).
- [34] CFOUR, a quantum chemical program package written by J.F. Stanton, J. Gauss, M.E. Harding, P.G. Szalay with contributions from A.A. Auer, R.J. Bartlett, U. Benedikt, C. Berger, D.E. Bernholdt, Y.J. Bomble, L. Cheng, O. Christiansen, M. Heckert, O. Heun, C. Huber, T.-C. Jagau, D. Jonsson, J. Jusélius, K. Klein, W.J. Lauderdale, D.A. Matthews, T. Metzroth, L.A. Mück, D.P. O'Neill, D.R. Price, E. Prochnow, C. Puzzarini, K. Ruud, F. Schiffmann, W. Schwalbach, C. Simmons, S. Stopkowicz, A. Tajti, J. Vázquez, F. Wang, J.D. Watts and the integral packages MOLECULE (J. Almlöf and P.R. Taylor), PROPS (P.R. Taylor), ABACUS (T. Helgaker, H.J. Aa. Jensen, P. Jørgensen, and J. Olsen), and ECP routines by A. V. Mitin and C. van Wüllen. For the current version, see <http://www.cfour.de>.
- [35] MRCC, a quantum chemical program suite written by Kállay, M and Rolik, Z and Ladjánszki, I and Szegedy, L and Ladóczki, B and Csontos, J and Kornis, B See also Z. Rolik and M. Kállay, *J. Chem. Phys.* 139, 094105 (2013), as well as: [www.mrcc.hu](http://www.mrcc.hu).
- [36] Pople, John A., Head-Gordon, Martin, and Raghavachari, Krishnan., Quadratic configuration interaction. A general technique for determining electron correlation energies, *J. Chem. Phys.*, 87(10), 5968 (1987).
- [37] Dunning, Thom H., Gaussian basis sets for use in correlated molecular calculations. I. The atoms boron through neon and hydrogen, *J. Chem. Phys.*, 90(2), 1007 (1989).
- [38] Koput, J and Peterson, Andrew A., Ab initio potential energy surface and vibrational-rotational energy levels of  $\text{X}2\Sigma^+ \text{CaOH}$ , *J. Phys. Chem. A*, 106, 9595 (2002).
- [39] Gauss, J., Ruud, K., and Kallay, M., Gauge-origin independent calculation of magnetizabilities and rotational g tensors at the coupled-cluster level. *J. Chem. Phys.*, 127(7), 074101 (2007).
- [40] Gauss, J., Ruud, K., and Helgaker, T., Perturbation-dependent atomic orbitals for the calculation of spin-rotation constants and rotational g tensors. *J. Chem. Phys.*, 105(7), 2804



- (1996).
- [41] Puzzarini, C., Stanton, J. F., and Gauss, J., Quantum-chemical calculation of spectroscopic parameters for rotational spectroscopy. *Int. Rev. Phys. Chem.*, 29(2), 273 (2010).
  - [42] Helgaker, T., Coriani, S., Jorgensen, P., Kristensen, K., Olsen, J., and Ruud, K., Recent advances in wave function-based methods of molecular-property calculations. *Chem. Rev.*, 112(1), 543 (2012).
  - [43] Gauss, J. and Sundholm, D., Coupled-cluster calculations of spin-rotation constants, *Mol. Phys.*, 91(3), 449 (1997).
  - [44] Jaszunski, M., Repisky, M., Demissie, T. B., Komorovsky, S., Malkin, E., Ruud, K., Garbacz, P., Jackowski, K., and Makulski, W., Spin-rotation and NMR shielding constants in HCl, *J. Chem. Phys.*, 139(23), 234302 (2013).
  - [45] Amano, T., The Zeeman effect and hyperfine interactions in  $J = 1-0$  transitions of  $\text{CH}^+$  and its isotopologues, *J. Chem. Phys.*, 133(24), 244305 (2010).
  - [46] Sundholm, D., Gauss, J., and Schäfer, A., Rovibrationally averaged nuclear magnetic shielding tensors calculated at the coupled-cluster level, *J. Chem. Phys.*, 105(24), 11051 (1996). 19
  - [47] Leibfried, D., et al., Creation of a six-atom ‘Schrödinger cat’ state, *Nature*, 438, 639 (2005).
  - [48] Morigi, G., Eschner, J., and Keitel, C. H., Ground state laser cooling using electromagnetically induced transparency, *Phys. Rev. Lett.*, 85, 4458 (2000).
  - [49] Roos, C. F., Monz, T., Kim, K., Riebe, M., Häffner, H., James, D. F. V., and Blatt, R., Nonlinear coupling of continuous variables at the single quantum level. *Phys. Rev. A*, 77, 040302(R) (2008).